

PoseGravity: Pose Estimation from Points and Lines with Axis Prior

Akshay Chandrasekhar
BallerTV

Abstract

This paper presents a new algorithm to estimate absolute camera pose given an axis of the camera’s rotation matrix. Current algorithms solve the problem via algebraic solutions on limited input domains. This paper shows that the problem can be solved efficiently by finding the intersection points of a hyperbola and the unit circle. The solution can flexibly accommodate combinations of point and line features in minimal and overconstrained configurations. In addition, the two special cases of planar and minimal configurations are identified to yield simpler closed-form solutions. Extensive experiments validate the approach.

1. Introduction

Estimating camera pose from image features and known 3D geometry is crucial for many computer vision applications such as augmented reality, visual odometry, and structure from motion. In certain scenarios, prior knowledge of the camera’s rotation axis is available (*e.g.* IMU measurement, detected vanishing point, or domain assumptions). Using this prior knowledge, the resulting problem reduces from six degrees of freedom (three for orientation, three for position) to four degrees of freedom as the rotation matrix only has only degree of freedom to rotate about the given axis. Some benefits of this simplified problem include reducing the minimum correspondences needed, improving the robustness of estimation to noise, and providing a quick initial solution for the general estimation problem. Previous solutions have been proposed that solve this problem for specific types of configurations or correspondences. In this paper, a fast and accurate algorithm is presented that generalizes the solution further by solving the problem for both point and line feature correspondences in minimal and overconstrained cases.

2. Relevant Work

Estimating camera pose from point correspondences is a well-studied problem. The first known solution was proposed by Grunert [3] in 1841 for the minimal case of three

projective point feature correspondences (P3P). Since then, numerous other analytical solutions have been proposed, typically framing the solutions as the roots of a quartic equation [6] [7]. Persson [12] took an alternative approach to the problem by formulating it as the intersection of two conic sections which involves finding a single root of a cubic equation instead.

Beyond the original P3P problem, solutions also emerged for the overconstrained pose estimation problem to solve for $n > 3$ points (PnP). EPnP [10] was one of the earliest solutions to the general PnP problem that ran $O(n)$ time for $n \geq 4$. Terzakis [17] provided a PnP solution by formulating the problem as a quadratic minimization problem followed by an iterative sequential quadratic program that was guaranteed to find the global minimum in a least squares sense.

Lines are another projective feature commonly used in the pose estimation problem. Analogous to the P3P and PnP problems are the P3L and PnL problems which are solved for the minimal and overconstrained line correspondence cases respectively. The former is solved by finding the roots to a degree 8 polynomial [19] [20], while the latter involves solving higher degree polynomials or large matrix nullspaces [13] [20]. Given the similarities between the point and line problems, notably the linear nature of the constraint equations, solving pose problems with both features has also been explored. Zhou [21] and Ramalingam [14] both solved point/line combinations for minimal cases via an octic polynomial. Ansar [1] solved for both points and lines for $n \geq 4$ in $O(n^2)$ time through a matrix nullspace approach, and Vakhitov [18] formulated a $O(n)$ solution by integrating the ends of line segments as points into existing PnP solvers.

With the rising ubiquity of integrated IMU sensors in devices such as smartphones, drones, and virtual reality gear, a measurement of gravity’s direction (or other heading) is easily accessible in many real world applications. As a result, integration of this measurement as a known prior into the estimation problem has received increased attention in recent years. Kukulova [8], Sweeney [16], and D’Alfonso [2] solved the problem in analytical form for two point correspondences (P2P) by solving a simple quadratic

equation. Horanyi [5] solved the overconstrained problem algebraically for $n \geq 3$ lines by boiling the problem down to the solutions of single cubic polynomial. Finally, Lecrosnier [9] also solved the problem for many lines by estimating the best unconstrained rotation and subsequently calculating the nearest valid rotation matrix.

2.1. Contributions

In this work, we attempt to further the state of the art by presenting a novel solution to the pose estimation with axis prior problem that has the following features:

- Accommodates combinations of point and line features in both minimal and overconstrained configurations
- Can be solved in closed form by finding the first root of a simplified cubic polynomial and the roots of two quadratic polynomials
- Represents solution domain without singularity
- Identifies and handles special cases with streamlined approaches, returning multiple valid solutions
- Runs efficiently in $O(n)$ time

In this paper, we will present the mathematical and empirical framework which justify these contributions.

3. Method

3.1. Problem Setup

The linear projective constraints that define the pose estimation problem given n point correspondences and m line correspondences are typically given by:

$$[\mathbf{p}_i]_{\times} (\mathbf{R}\mathbf{d}_i + \mathbf{T}) = 0 \quad (1)$$

$$\mathbf{n}_j \cdot (\mathbf{R}\mathbf{m}_j + \mathbf{T}) = 0 \quad (2)$$

$$\mathbf{n}_j \cdot (\mathbf{R}\mathbf{v}_j) = 0 \quad (3)$$

$$\forall i \in 0 \dots n - 1 \quad \forall j \in 0 \dots m - 1$$

where \mathbf{R} and \mathbf{T} are the rotation matrix and translation of the camera's pose to be estimated, $\mathbf{p} = [p_x, p_y, p_z]^T$ and $\mathbf{d} = [d_x, d_y, d_z]^T$ are the given 2D and 3D point correspondences respectively, $\mathbf{n} = [n_x, n_y, n_z]^T$ is a normal vector defining the 2D line, and $\mathbf{m} = [m_x, m_y, m_z]^T$ and $\mathbf{v} = [v_x, v_y, v_z]^T$ are the points and line directions defining the 3D lines respectively. The 2D features are assumed to be in normalized coordinates (calibrated camera). $[\mathbf{p}]_{\times}$ denotes the skew-symmetric matrix created from vector \mathbf{p} representing a cross product. It is well known that equation 1 yields two algebraically independent linear equations for each point correspondence ($[\mathbf{p}]_{\times}$ is a matrix of rank 2),

and equations 2 and 3 each yield an algebraically independent linear equation for each line correspondence. Therefore, each line or point correspondence gives two pieces of information about the problem.

We assume our axis prior is the world y-axis, and our measurement of that axis is given as a gravity vector (world y-axis in camera frame). Otherwise, we can always rotate the 2D or 3D correspondences to be aligned with such a reference frame. We first introduce a new coordinate frame rotation denoted by $\mathbf{R}_{\mathbf{g}}$ such that the unit-norm gravity measurement $\mathbf{g} = [g_x, g_y, g_z]^T$ when rotated by $\mathbf{R}_{\mathbf{g}}$ is aligned with the camera's y-axis. Note that the choice of $\mathbf{R}_{\mathbf{g}}$ is not unique. One way to define $\mathbf{R}_{\mathbf{g}}$ from \mathbf{g} that only uses simple arithmetic (via axis-angle formula for rotation matrices) is:

$$\mathbf{R}_{\mathbf{g}}\mathbf{g} = \begin{pmatrix} 0 \\ 1 \\ 0 \end{pmatrix} \quad (4)$$

$$\mathbf{R}_{\mathbf{g}} = \begin{bmatrix} \frac{g_z^2}{1+g_y} + g_y & -g_x & \frac{-g_x g_z}{1+g_y} \\ g_x & g_y & g_z \\ \frac{-g_x g_z}{1+g_y} & -g_z & \frac{g_x^2}{1+g_y} + g_y \end{bmatrix} \quad (5)$$

The above is undefined for $g_y = -1$ where we can choose $\mathbf{R}_{\mathbf{g}}$ to be any 180 degree rotation about an axis in the plane $y = 0$. Introducing this coordinate transformation allows us to decompose the total rotation \mathbf{R} into a 2D rotation about the y-axis $\tilde{\mathbf{R}}$ followed by $\mathbf{R}_{\mathbf{g}}^T$. This isolates the remaining degree of freedom left to be estimated in the rotation matrix.

$$\tilde{\mathbf{R}} = \begin{bmatrix} x & 0 & y \\ 0 & 1 & 0 \\ -y & 0 & x \end{bmatrix} \quad (6)$$

$$\mathbf{R} = \mathbf{R}_{\mathbf{g}}^T \tilde{\mathbf{R}} \quad (7)$$

Here, x and y are the cosine and sine of the angle of rotation about the y-axis related by the elementary identity $x^2 + y^2 = 1$. Equations 1 to 3 are transformed by $\mathbf{R}_{\mathbf{g}}$, so we can reframe the problem constraints to estimate $\tilde{\mathbf{R}}$.

$$\mathbf{R}_{\mathbf{g}}\mathbf{p}_i = \mathbf{p}'_i \quad (8)$$

$$\mathbf{R}_{\mathbf{g}}\mathbf{n}_j = \mathbf{n}'_j \quad (9)$$

$$\mathbf{R}_{\mathbf{g}}\mathbf{T} = \tilde{\mathbf{T}} \quad (10)$$

$$[\mathbf{p}'_i]_{\times} (\tilde{\mathbf{R}}\mathbf{d}_i + \tilde{\mathbf{T}}) = 0 \quad (11)$$

$$\mathbf{n}'_j \cdot (\tilde{\mathbf{R}}\mathbf{m}_j + \tilde{\mathbf{T}}) = 0 \quad (12)$$

$$\mathbf{n}'_j \cdot (\tilde{\mathbf{R}}\mathbf{v}_j) = 0 \quad (13)$$

$$\forall i \in 0 \dots n - 1 \quad \forall j \in 0 \dots m - 1$$

From here, the prime and tilde notation are dropped for clarity as the problem focuses on estimating the rotation and translation in this transformed space.

3.2. Constrained Least Squares Formulation

If we have two independent 2D-3D correspondences, equations 11 to 13 hold exactly. However, if we have more than two, then the left and right sides of those equations may not be equal, and we would seek to estimate the best \mathbf{R} and \mathbf{T} in the least squares sense. Following the formulation of [17], we note that a rotation of a vector \mathbf{u} can be equivalently rewritten in the form:

$$\begin{bmatrix} u_x & u_y & u_z & 0 & 0 & 0 & 0 & 0 & 0 \\ 0 & 0 & 0 & u_x & u_y & u_z & 0 & 0 & 0 \\ 0 & 0 & 0 & 0 & 0 & 0 & u_x & u_y & u_z \end{bmatrix} \text{vec}(\mathbf{R}) \quad (14)$$

where $\text{vec}(\mathbf{R})$ is a row-flattened vector representation of \mathbf{R} . In our case, we only have 3 unique elements in our rotation matrix, so we can simplify the expression as:

$$\mathbf{R}\mathbf{u} = \begin{bmatrix} u_x & u_z & 0 \\ 0 & 0 & u_y \\ u_z & -u_x & 0 \end{bmatrix} \begin{bmatrix} x \\ y \\ 1 \end{bmatrix} = \mathbf{U}\mathbf{r} \quad (15)$$

We refer to \mathbf{U} as the matrix representation of vector \mathbf{u} . Squaring equations 11 to 13 and adding them together for all points and lines, we can work the equations into the following optimizable objective function:

$$\min_{\mathbf{r}, \mathbf{T}} \sum_i (\mathbf{A}_i^p \mathbf{r} + \mathbf{T})^T \mathbf{Q}_i^p (\mathbf{A}_i^p \mathbf{r} + \mathbf{T}) + \sum_j (\mathbf{A}_j^l \mathbf{r} + \mathbf{T})^T \mathbf{Q}_j^l (\mathbf{A}_j^l \mathbf{r} + \mathbf{T}) + \delta^2 \sum_j (\mathbf{V}_j \mathbf{r})^T \mathbf{Q}_j^l (\mathbf{V}_j \mathbf{r}) \quad (16)$$

\mathbf{A}_i^p , \mathbf{A}_j^l , \mathbf{V}_l are the matrix representations of \mathbf{p}_i , \mathbf{m}_j , and \mathbf{v}_j respectively and \mathbf{Q}_i^p and \mathbf{Q}_j^l are $[\mathbf{p}_i]_{\times}^T [\mathbf{p}_i]_{\times}$ and $\mathbf{n}_j \mathbf{n}_j^T$ respectively. δ is a scaling factor (see Suppl. Mat. for details). We observe that this sum of squared linear equations is non-negative and convex with respect to unconstrained \mathbf{T} . Taking the derivative of the objective function with respect to \mathbf{T} and setting it to 0, we can solve for the globally minimizing value of \mathbf{T} given \mathbf{r} :

$$\begin{aligned} \mathbf{T} &= \mathbf{S}\mathbf{r} \\ &= \left(\sum_i \mathbf{Q}_i^p + \sum_j \mathbf{Q}_j^l \right)^{-1} \left(\sum_i \mathbf{Q}_i^p \mathbf{A}_i^p + \sum_j \mathbf{Q}_j^l \mathbf{A}_j^l \right) \mathbf{r} \quad (17) \end{aligned}$$

If we are given at least two points, three lines, or a point and a line (objects assumed linearly independent), then $\sum_i \mathbf{Q}_i^p + \sum_j \mathbf{Q}_j^l$ is guaranteed to be invertible (Proof in Suppl. Mat.). Substituting this value of \mathbf{T} back into the objective function and consolidating the terms, we can end up with the following simplified constrained quadratic min-

imization problem:

$$\Omega = \sum_i (\mathbf{A}_i^p + \mathbf{S})^T \mathbf{Q}_i^p (\mathbf{A}_i^p + \mathbf{S}) +$$

$$\sum_j (\mathbf{A}_j^l + \mathbf{S})^T \mathbf{Q}_j^l (\mathbf{A}_j^l + \mathbf{S}) + \delta^2 \sum_j \mathbf{v}_j^T \mathbf{Q}_j^l \mathbf{v}_j \quad (18)$$

$$\min_{\mathbf{r}} \mathbf{r}^T \Omega \mathbf{r} \text{ s.t. } x^2 + y^2 = 1 \quad (19)$$

Note that Ω takes the form of a sum of matrices $B^T B$, so it is a symmetric positive semidefinite matrix. Also, note that \mathbf{r} takes on the form $[x, y, 1]^T$, so the objective function's level sets can therefore be interpreted as conic sections in the x - y plane over the projective space. We thus refer to Ω as the *loss conic*.

3.3. Solution

The constrained optimization problem in equation 19 can be solved in closed form by optimizing the associated Lagrangian:

$$\min_{x,y} f(x,y) + \lambda(x^2 + y^2 - 1) \quad (20)$$

where $f(x,y)$ is the expanded polynomial form of $\mathbf{r}^T \Omega \mathbf{r}$. Taking the partial derivatives with respect to x , y , and λ :

$$\frac{df}{dx} + 2\lambda x = 0 \quad (21)$$

$$\frac{df}{dy} + 2\lambda y = 0 \quad (22)$$

$$x^2 + y^2 = 1 \quad (23)$$

We can eliminate λ by multiplying the first equation by y and subtracting the second equation multiplied by x . This yields a new equation which can also be written in conic form that we refer to as the *derivative conic*:

$$\begin{bmatrix} x \\ y \\ 1 \end{bmatrix}^T \begin{bmatrix} -2\Omega_{0,1} & \Omega_{0,0} - \Omega_{1,1} & -\Omega_{1,2} \\ \Omega_{0,0} - \Omega_{1,1} & 2\Omega_{0,1} & \Omega_{0,2} \\ -\Omega_{1,2} & \Omega_{0,2} & 0 \end{bmatrix} \begin{bmatrix} x \\ y \\ 1 \end{bmatrix} = \mathbf{r}^T \Lambda \mathbf{r} = 0 \quad (24)$$

This conic is a hyperbola in general cases. The remaining equation to use is 23 which specifies the equation of a circle, a conic itself that can be written as:

$$\begin{bmatrix} x \\ y \\ 1 \end{bmatrix}^T \begin{bmatrix} 1 & 0 & 0 \\ 0 & 1 & 0 \\ 0 & 0 & -1 \end{bmatrix} \begin{bmatrix} x \\ y \\ 1 \end{bmatrix} = \mathbf{r}^T \Phi \mathbf{r} = 0 \quad (25)$$

Thus, the problem has come down to finding the intersection of two conics. It is well known that two conics can have up to four unique points of intersection. Note that the derivative conic goes through the plane origin, so generally

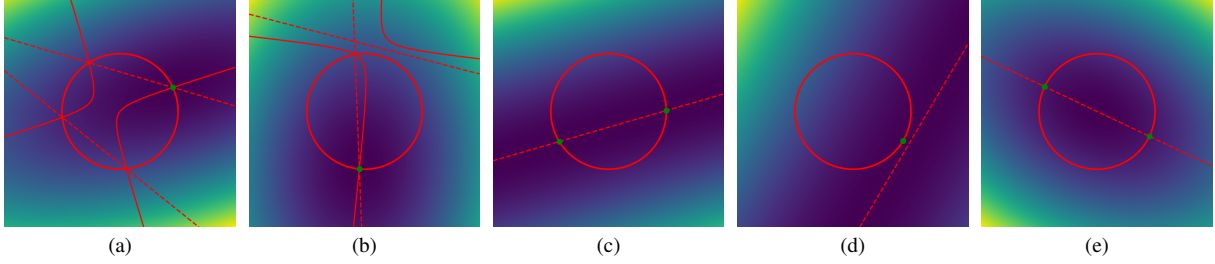


Figure 1. Examples of problem loss spaces with relevant objects in the x - y plane. The darker regions correspond to lower loss values over objective function Ω , the red circle is the unit circle, and the green dots are the global minimums of Ω on the unit circle. (a), (b) show general problems. The red hyperbola corresponds to the derivative conic Λ . The dashed red lines are the lines constituting the degenerate conic Σ . (a) has four intersections (stationary points) while (b) only has two. (c), (d) show minimal configurations. The dashed line here is the zero level curve of the degenerate loss conic Ω (single double line). In (c), the line intersects the circle for two solutions while in (d) a solution is recovered from an infeasible problem with no intersections. (e) shows a planar configuration. The dashed line here is the eigenvector corresponding to the smallest eigenvalue of Ω' . Note this line goes through the origin.

there are at least two intersections with the unit circle in our case. Solving for those points is often formulated as finding the roots to a univariate quartic function. Instead, we find a more efficient geometric approach by following the algorithm laid out in [15]. First we generate a pencil of conics (linear combination of conics):

$$\mu\Lambda + \gamma\Phi = 0, \mu, \gamma \in \mathbb{R} \quad (26)$$

It can be seen that any intersection point of our two conics also lies on the pencil of conics. We search this pencil for a specific conic that will be easier to intersect with our original conics. That conic is a degenerate conic (*i.e.* a rank-deficient conic interpreted as a pair of lines or single double line) which goes through the desired points of intersection. Since equation 26 is homogeneous, we can divide the pencil by μ so that the coefficient of Λ is 1 and γ takes on another scalar value. We note that $\mu = 0$ is never a solution as Φ is full-rank and constant for all problems. Using the condition that a rank-deficient matrix has a determinant of 0, we can solve for a value γ that yields a degenerate conic:

$$\det(\Lambda + \gamma\Phi) = \det(\Sigma) = 0 \quad (27)$$

This yields a cubic equation in γ :

$$\gamma^3 + a\gamma + b = 0 \quad (28)$$

$$a = \Lambda_{0,2}^2 + \Lambda_{1,2}^2 - \Lambda_{0,0}^2 - \Lambda_{0,1}^2 \quad (29)$$

$$b = \Lambda_{0,0}(\Lambda_{1,2}^2 - \Lambda_{0,2}^2) - 2\Lambda_{0,1}\Lambda_{0,2}\Lambda_{1,2} \quad (30)$$

The formulated cubic equation has several noteworthy properties. Being a cubic, the equation can be solved in closed form via Cardano's method or by other numerical methods. The equation is *monic* (coefficient of the cubic term is 1) so we avoid the numerical stability issues when dealing with very small cubic coefficients. The equation is also a

depressed cubic (quadratic term is absent) which reduces the computational complexity of solving it. Furthermore, computing the coefficients a and b from the loss conic involves just a handful of operations. Finally, only the first real root is needed since a single γ value can satisfy 27. Since cubic equations have at least one real root, we are guaranteed to always have a solution.

After obtaining a real root γ_0 , we can retrieve the degenerate conic Σ . We then decompose this conic into the lines that constitute it. The procedure is described briefly in Algorithm 1 (for more details, see [15]). Note that we can determine the rank of Σ easily in the first step since it is generally known for 3×3 singular matrices that the $\text{rank}(\text{adj}(\Sigma)) = 1$ only if $\text{rank}(\Sigma) = 2$. Otherwise, $\text{rank}(\text{adj}(\Sigma)) = 0$. Thus, the adjugate is checked to be the zero matrix, and the algorithm can proceed accordingly.

We can intersect the decomposed lines with either of our original conics to obtain the solutions (Figures 1a, 1b). We choose the circle Φ since it is a simpler object. Intersecting a line with a circle leads to a quadratic equation which is solved in closed form. Each line gives up to two intersections, and two lines give four total possible intersections, the same as a quartic equation would in the purely algebraic approach. Each intersection corresponds to either a local minimum, maximum, or saddle point of 20. Thus, we plug each real intersection obtained into 19 and select the ones with the lowest loss value to find the global minimum.

3.4. Recovering \mathbf{R} and \mathbf{T}

It can be seen that among the four possible stationary points, we may have at most two unique minimizing points (x, y) . If their loss function value is the same, then both points are valid global solutions. For each solution obtained, we can plug it back into equation 6 to obtain $\tilde{\mathbf{R}}$ and use equation 7 to obtain our original total rotation \mathbf{R} . We can similarly plug in each solution to equation 17 to obtain

Algorithm 1 Decompose Degenerate Conic into Lines

```
1: function DECOMPOSECONIC( $\Sigma$ )
2:    $G = \text{adjugate}(\Sigma)$ 
3:   if  $\text{rank}(G) = 0$  then                                 $\triangleright \text{rank}(\Sigma) = 1$ 
4:      $l_1 \leftarrow$  nonzero row of  $\Sigma$ 
5:     return  $l_1$ 
6:   else                                                 $\triangleright \text{rank}(\Sigma) = 2$ 
7:      $\beta \leftarrow$  a nonzero diagonal element of  $G$ 
8:      $z \leftarrow$  row of  $G$  containing  $\beta$ 
9:      $z = \frac{1}{\sqrt{-\beta}}z$ 
10:     $H = \Sigma + [z]_{\times}$ 
11:     $l_1, l_2 \leftarrow$  row, column of nonzero element of  $H$ 
12:    return  $l_1, l_2$ 
```

$\tilde{\mathbf{T}}$ and use equation 10 to recover the final translation \mathbf{T} .

3.5. Minimal Configurations

A special case exists for minimal configurations (two points or a line and a point) as $\text{rank}(\Omega)$ will be at most 1 (Proof in Suppl. Mat.). In this case, the objective is simplified to:

$$\min_{\mathbf{r}} (l^T \mathbf{r})(l^T \mathbf{r}) \text{ s.t. } x^2 + y^2 = 1 \quad (31)$$

for some vector l . The equation has exact solutions of form $l \cdot \mathbf{r} = 0$ *i.e.* l is line of (x, y) solutions to the unconstrained problem whose intersection with the unit circle gives us the exact solution to our constrained problem (Figure 1c). Thus, we can find l by decomposing Ω directly, bypassing most of the algorithm laid out previously. The intersection of l with the unit circle is a simple quadratic equation which can give up to two unique real solutions, each of which is a global solution.

In certain cases (*e.g.* infeasible configuration geometry, large noise, *etc.*), it is possible to observe that the line l does not intersect the circle at all. In these cases, we can still recover the best (*i.e.* loss-minimizing) feasible solution by taking the nearest point to the line on the circle (Proof in Suppl. Mat.) (Figure 1d).

3.6. Planar Configurations

Another special case is when all of the 3D features lie in the plane $y = 0$ (or any plane orthogonal to the prior axis as the problem may be translated to this plane). This arises when observing a gravity measurement and detecting features on a ground plane (*e.g.* identifying markers on a street in autonomous navigation). If we follow the construction of Ω , we see that in such a scenario, the last row and column will vanish making the loss conic singular. Removing the last row/column from Ω and \mathbf{r} in equation 19 converts the problem into a minimization of a quadratic function over

the unit circle:

$$\mathbf{r}'^T \Omega' \mathbf{r}' = \begin{bmatrix} x \\ y \end{bmatrix}^T \begin{bmatrix} \Omega_{0,0} & \Omega_{0,1} \\ \Omega_{0,1} & \Omega_{1,1} \end{bmatrix} \begin{bmatrix} x \\ y \end{bmatrix} \quad (32)$$

$$\min_{\mathbf{r}'} \mathbf{r}'^T \Omega' \mathbf{r}' \text{ s.t. } \|\mathbf{r}'\| = 1 \quad (33)$$

The solution to this is well known as the eigenvector corresponding to the smallest eigenvalue of Ω' . Since Ω' is a 2x2 matrix, the solution can be expressed simply in closed form as:

$$\mathbf{k} = \left[-2\Omega_{0,1}, \Omega_{0,0} - \Omega_{1,1} + \sqrt{(\Omega_{0,0} - \Omega_{1,1})^2 + 4\Omega_{0,1}^2} \right] \quad (34)$$

$$\mathbf{r}' = \frac{\mathbf{k}}{\|\mathbf{k}\|} \quad (35)$$

Remarkably, the solution is yielded without explicitly solving any polynomials. Note the above assumes $\Omega_{0,1} \neq 0$ which if not valid can be easily handled. Eigenvectors are only unique up to a scale, so if \mathbf{r}' is a valid solution, $-\mathbf{r}'$ is as well. Such planar configurations therefore always yield two solutions, even in overconstrained configurations. Furthermore, the solutions are related as they form an antipodal pair on the unit circle (Figure 1e). Compared to the conic decomposition approach, this eigenvector solution is explicit and efficiently yields the two minimizing points directly instead of the general four stationary points of 20.

4. Experiments

Synthetic pose experiments are conducted to evaluate the approach and compare to others. Three input configurations in particular are considered: image plane detections, spherical detections, and planar scene configurations.

4.1. Experiment Setup

For each problem, the ground truth rotation is sampled randomly as a quaternion from the unit sphere S^3 , and translations are sampled randomly as a unit vector on S^2 . The ground truth gravity vector measurement is taken as the second column of the rotation matrix (world y-axis). In image plane detection problems, x and y image point coordinates are uniformly sampled between -1 and 1 in normalized coordinates with $z = 1$. They are then inversely transformed by the sampled rotation and translation and projected into 3D space by a uniformly random depth between 0.01 and 100. Spherical detection problems are generated similarly but the 2D detections are first sampled uniformly from the sphere S^2 instead of the image plane to simulate wide-angle cameras. Finally, planar scene problems are generated similarly to the spherical detections case except the transformed points are projected onto the 3D plane $y = 0$. Image points here are checked to be consistent with

Algorithm 2 Overview of Algorithm

Input 2D points \mathbf{p}_i , 3D points \mathbf{d}_i , 2D lines \mathbf{n}_j , 3D line directions \mathbf{v}_j , 3D line points \mathbf{m}_j , gravity vector \mathbf{g}

Output Estimated camera poses \mathbf{R} and \mathbf{T}

```
1: function POSEGRAVITY
2:   Create  $\mathbf{R}_g$  from  $\mathbf{g}$  using 5
3:   Rotate detections  $\mathbf{p}'_i = \mathbf{R}_g \mathbf{p}_i$ ,  $\mathbf{n}'_j = \mathbf{R}_g \mathbf{n}_j$ 
4:   Generate  $\Omega$  using 14 to 18
5:   if  $\Omega_{:, -1} = \mathbf{0}$  then                                     ▷ Planar
6:      $\mathbf{r}_0 \leftarrow$  34, 35
7:      $\text{sol} \leftarrow \{\mathbf{r}_0, -\mathbf{r}_0\}$ 
8:   else if  $\text{rank}(\Omega) = 1$  then                                 ▷ Minimal
9:      $l_1 \leftarrow$  DECOMPOSECONIC( $\Omega$ )
10:     $\text{sol} \leftarrow$  intersect  $l_1$  with circle
11:    if  $\text{sol} = \emptyset$  then
12:       $\text{sol} \leftarrow$  closest point on circle to  $l_1$ 
13:   else                                                         ▷ General
14:      $a \leftarrow$  29,  $b \leftarrow$  30
15:      $\gamma_0 \leftarrow$  solve real root of 28
16:      $\Sigma = \Lambda + \gamma_0 \Phi$ 
17:      $l_1, l_2 \leftarrow$  DECOMPOSECONIC( $\Sigma$ )
18:      $\mathbf{r} \leftarrow$  intersect  $l_1, l_2$  with circle
19:      $\text{loss} = \{\mathbf{r}_k^T \Omega \mathbf{r}_k \mid \forall \mathbf{r}_k \in \mathbf{r}\}$ 
20:      $k^* = \text{argmin } \text{loss}$ 
21:      $\text{sol} \leftarrow \{\mathbf{r}_k \mid \forall k : \text{loss}_k = \text{loss}_{k^*}\}$ 
22:    $\mathbf{R} \leftarrow$  6, 7 for each  $\mathbf{r}_k \in \text{sol}$ 
23:    $\mathbf{T} \leftarrow$  10, 17 for each  $\mathbf{r}_k \in \text{sol}$ 
```

cheirality constraints. In order to maintain a random scale, the translation in the planar scene case is scaled by a sampled factor between 0.01 and 100. Line features in 2D and 3D are created from pairs of points treated by the procedure above for each case.

To simulate noisy measurements and detections, gravity vector measurement noise and 2D detection noise are added. For the former, the gravity vector measurement is rotated around a random axis by a normally distributed angle θ_{noise} in degrees. For the latter, independent Gaussian noise ϵ_{noise} is added to each component of each 2D feature.

The accuracy is evaluated by measuring the error in the estimated rotation and translation separately. The rotation error is given as the angle in degrees between the estimated rotation and the ground truth rotation. The translation error is simply the Euclidean distance between the estimated translation and the ground truth translation.

$$\theta_{err} = \cos^{-1}\left(\frac{\text{Tr}(\mathbf{R}_{gt}^T \mathbf{R}_{est}) - 1}{2}\right) \quad (36)$$

$$T_{err} = \|\mathbf{T}_{gt} - \mathbf{T}_{est}\| \quad (37)$$

In the case that more than one solution is returned, the solution with the lowest rotation error is used.

4.2. Implementation

We directly compare the performance (speed and accuracy) of the proposed solver against several existing solutions. Specifically, VPnL [9] and gPnLup [5] were chosen as comparative solvers accommodating $n \geq 3$ line features and an axis prior. Sweeney [16] was chosen as a comparative P2P solution solving the two point minimal configuration with axis prior. All three were re-implemented and optimized in C++ in a similar style as our algorithm which minimized compute and avoided external libraries. For VPnL, the VPnL_LS algorithm was used in order to compare analytic solutions, and the SVD operation which was used for estimating nearest rotation was replaced by the FOAM method in [11] which yielded a significant compute improvement for the same accuracy. For gPnLup, the best cubic root is selected by lowest projective error (*i.e.* square of equations 1 to 3) akin to the original implementation. gPnLup as presented does not handle multiple solutions from a planar configuration properly as there is typically a single global minimum for its loss among the roots. Thus, we also return any second best root as well for planar configurations for fairer comparison.

Furthermore, Lambda Twist [12] and SQPnP [17] are also compared as general P3P and PnP solutions respectively to illustrate the utility of axis prior solutions. Production implementations in C++ were taken from the paper authors. Note that SQPnP requires the use of external library Eigen to perform linear algebra operations.

All experiments were compiled in C++ 14 with Apple clang 13.0 using the compiler flags `-O3` and `-funroll`. For each experiment, at least 100k trials are run and the median for each metric is reported.

5. Discussion

Figure 2 illustrates the proposed solver’s performance against gravity vector measurement noise for various input types. The algorithm performs better on spherical configurations than image plane configurations, particularly on translation error with large numbers of features. It achieves its best performance on planar configurations where the streamlined solution yields much better estimates overall, especially for smaller input sizes. While experiments with three points fared comparably to experiments with three lines on rotation error, the former had much lower translation errors in all cases, suggesting that point features are more favorable for our approach.

Table 1 compares the results of the proposed algorithm in the minimal two point case against the competing P2P solution [16]. Without any recovery of minimal solutions, the algorithm results are virtually identical. However, the algorithm with recovery is able to always return a valid solution. These recovered solutions are noisy by definition, so

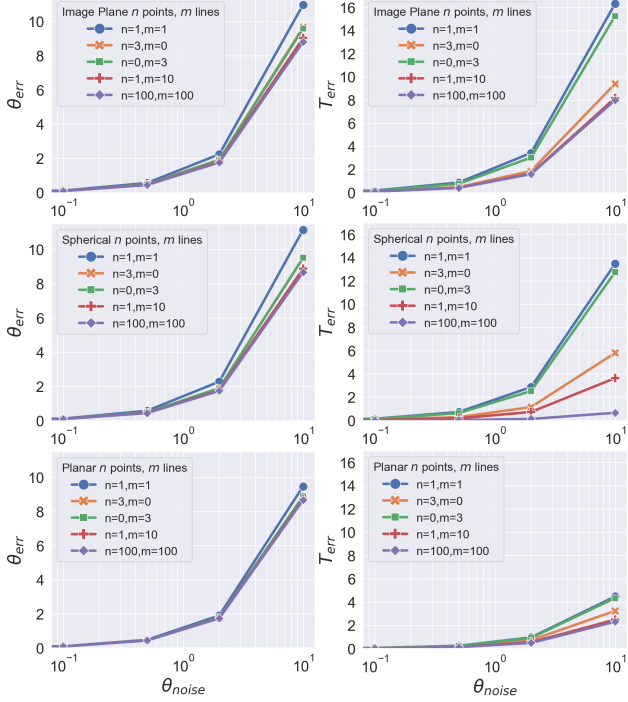


Figure 2. Performance of proposed algorithm on various input types, configurations, and levels of θ_{noise} . Left: rotation error θ_{err} , Right: translation error T_{err} . Configurations - Top: Image Plane, Middle: Spherical, Bottom: Planar.

ϵ_{noise}	Algorithm	# With Sol.	θ_{err}	T_{err}
1e-3	P2P [16]	989615	0.090848	0.14768
	Ours*	989615	0.090848	0.14768
	Ours	1000000	0.092204	0.14968
0.01	P2P [16]	967218	0.87618	1.4285
	Ours*	967218	0.87618	1.4285
	Ours	1000000	0.91441	1.4809
0.1	P2P [16]	901866	7.8776	12.948
	Ours*	901866	7.8776	12.948
	Ours	1000000	8.6215	13.846

Table 1. Results of a million trials on two point inputs in image plane configuration for varying detection noise levels. Column values are number of trials with at least one solution returned, rotation error, and translation error. * denotes proposed algorithm without solution recovery.

their inclusion marginally increases the reported error proportional to their amount in each batch of trials.

Figure 3 shows the comparison of the algorithm against the baseline PnP solvers. These plots identify the regions in which the gravity vector solution acts as an effective regularizer against noise. For small amounts of points, we see that the algorithm generally outperforms the P3P solution when $\epsilon_{noise} > 0.01$ and $\theta_{noise} < 1.5$ degrees or

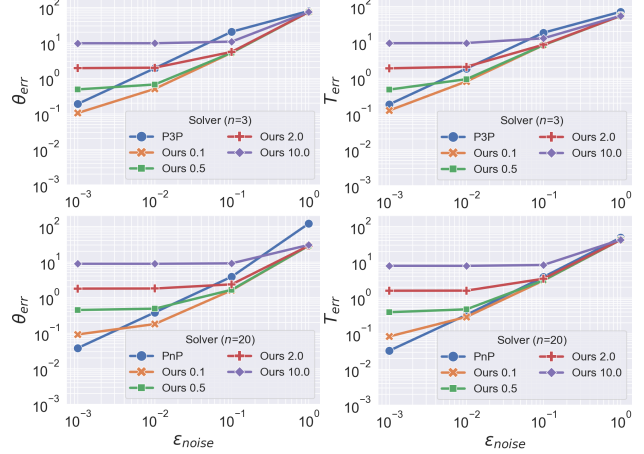


Figure 3. Performance of the algorithm in image plane configuration under different levels of θ_{noise} compared to general solvers for various levels of ϵ_{noise} . Left: rotation error θ_{err} , Right: translation error T_{err} . Top: $n = 3$ points, Bottom: $n = 20$ points. For our solvers, the number in legend refers to standard deviation of θ_{noise} applied. P3P from [12], PnP from [17].

when $\epsilon_{noise} > 0.1$. Note that with P3P, we can get up to four valid solutions while our algorithm returns at most two (usually just one for three input points). For larger numbers of points, the algorithm outperforms the PnP solution in the region where $\epsilon_{noise} > 0.05$ and $\theta_{noise} < 1$ degree.

Table 2 shows a direct comparison of the algorithm against other axis prior solutions for various experiments. Overall, the proposed solver is competitive with other approaches, having the lowest rotation error for majority of experiments. It ranked at least second best in nearly all cases, still managing to perform the best on a sizable subset of the each experiment’s trials. The algorithm stands out in planar configurations with its particularly low rotation errors. This can be attributed to the specialized solution implemented for this unique case which, if not handled properly, can result in incorrect solutions. In contrast, the formulation of gPnP has an objective that’s biased by the rotation angle being solved for. This is apparent in Table 2 as it fails to lead in any experiment and is less competitive at higher noise levels. On the other hand, VPnLLS shows a strong performance on translation estimates and image plane scenes with its formulation based on Plücker line coordinates. In other scenes, it can yield less accurate rotation estimates, especially in planar configurations.

Finally, tables 3a and 3b compare runtime timings of each algorithm. For point-based solvers, our algorithm outperforms other solutions which feature more complicated formulations. SQnPn in particular has many expensive operations including a 9x9 matrix eigendecomposition. For line-based solvers, the algorithms are comparable for small numbers of lines. For larger line amounts, the proposed

ϵ	Config	$m = 3$			$m = 20$			$m = 250$		
		gPnPup	VPnL_LS	Ours	gPnPup	VPnL_LS	Ours	gPnPup	VPnL_LS	Ours
1e-3	Image	0.040/0.220	0.036/0.192	0.040/0.219	0.014/0.049	0.012/0.036	0.015/0.048	0.004/0.014	0.003/0.010	0.004/0.013
	Spherical	0.041/0.143	0.047/ 0.109	0.040/0.143	0.015/0.034	0.015/ 0.019	0.014/0.034	0.004/0.009	0.004/ 0.005	0.004/0.009
	Planar	0.027/0.126	0.047/ 0.119	0.027/0.126	0.010/0.027	0.015/ 0.025	0.010/0.027	0.003/0.008	0.004/ 0.007	0.002/0.008
0.01	Image	0.413/2.23	0.363/1.94	0.405/2.21	0.156/0.506	0.120/0.364	0.152/0.488	0.049/0.148	0.033/0.102	0.043/0.139
	Spherical	0.415/1.46	0.470/ 1.10	0.409/1.45	0.157/0.348	0.152/ 0.190	0.146/0.344	0.050/0.098	0.042/ 0.052	0.041/0.097
	Planar	0.279/1.25	0.480/ 1.22	0.276/1.24	0.116/0.283	0.153/ 0.255	0.105/0.277	0.036/0.083	0.042/ 0.077	0.030/0.081
0.1	Image	4.96/25.0	4.05/17.8	4.24/22.4	2.46/6.28	1.26/3.79	1.53/5.31	1.84/4.00	0.351/1.07	0.434/3.30
	Spherical	5.00/16.3	4.91/ 10.2	4.29/14.6	2.45/3.78	1.55/ 1.96	1.47/3.40	1.81/1.06	0.433/ 0.540	0.415/0.965
	Planar	3.09/13.2	5.23/ <u>13.1</u>	2.78/12.3	2.30/4.49	1.63/ <u>3.17</u>	1.08/2.87	1.51/1.80	0.457/ <u>1.68</u>	0.326/1.16
1	Image	81.2/89.9	<u>76.5/48.0</u>	74.6/85.3	80.9/51.2	<u>50.8/39.8</u>	36.9/47.0	80.6/48.8	<u>17.5/18.6</u>	7.67/43.9
	Spherical	81.2/77.1	72.5/32.9	<u>74.0/71.8</u>	81.0/22.6	<u>41.7/17.1</u>	34.1/19.9	81.2/6.87	<u>12.3/6.62</u>	7.12/5.95
	Planar	51.1/76.7	73.4/ 56.0	<u>30.4/68.1</u>	83.7/45.6	<u>44.4/39.7</u>	17.3/29.3	88.7/42.4	14.0/ <u>25.6</u>	6.30/25.4

Table 2. Comparison against other axis prior line-based solvers for varying line amounts m , ϵ_{noise} , and problem configurations. Values reported as θ_{err}/T_{err} pairs. Bold font indicates best value, underline indicates next best value among solvers for θ_{err} and T_{err} separately. gPnPup from [5], VPnL_LS from [9].

n	PnP	Ours	Ours (Planar)
2	0.583	0.416	0.375
3	1.959	0.791	0.417
20	444.876	1.416	1.042
250	689.582	9.625	9.291

(a)

m	gPnPup [5]	VPnL_LS [9]	Ours	Ours (Planar)
3	0.542	0.834	0.792	0.458
20	1.625	2.292	1.583	1.167
250	15.542	21.416	11.208	10.834

(b)

Table 3. Median algorithm runtimes in microseconds for a) points and b) lines. (Planar) indicates planar configuration used instead of image plane. For PnP timings, P2P [16] used for $n = 2$, Lambda Twist [12] used for $n = 3$, SQPnP [17] used for $n > 3$.

solver scales more efficiently due to estimating rotation and translation simultaneously with a single pass over the inputs. The other solvers require at least two iterations (three for gPnPup with multiple cubic roots) due to their sequential estimation of rotation followed by translation. Furthermore, the proposed algorithm’s streamlined solution for planar configurations, a case ignored by other approaches, yields the best timings in all experiments.

6. Real World Example

We briefly showcase the proposed algorithm’s utility with a real world example. Specifically, we perform the task of sports field registration on youth and amateur basketball court images. Solving this task allows us to know how the

camera is placed in the real world relative to the court which in turn enables a mapping between the 2D image and 3D scene. This is useful for sports analysis, autonomous monitoring of camera setups, and overlaying augmented reality graphics. We capture the court images with a mobile device equipped with a superfish-eye lens and mounted on top of a tripod. The general image calibration is known (with some distortion noise between individual setups), and the device is equipped with sensors capable of gravity measurements. For this example, we assume the court’s size and backboard positions follow standard high school court specifications.

Given the significant appearance variation across amateur and youth basketball courts, pose estimation is conducted using a small set of general correspondences. For this task, we employ neural networks to detect three key points: the locations where the hoop rims attach to the backboards and the center of the far sideline on the ground as highlighted in Figure 4a. Running our algorithm on all three points and the gravity vector measurement yields qualitatively good results as shown in Figure 4c. In some cases, one of the three points may be unavailable due to occlusion, poor detection quality, or other factors. Estimation in these cases can still proceed with our algorithm using the remaining two correspondences and the gravity vector measurement which constitute a minimal configuration. While more affected by noise without the third correspondence, leveraging the gravity vector still allows a reasonable estimate to be computed as shown in Figure 4b.

Occasionally, we fail to detect at least two correspondences in which case manual annotations are used instead. A mobile interface is provided that allows users to annotate the edges of the court by tracing over the captured image with their finger, generating a noisy point contour of the

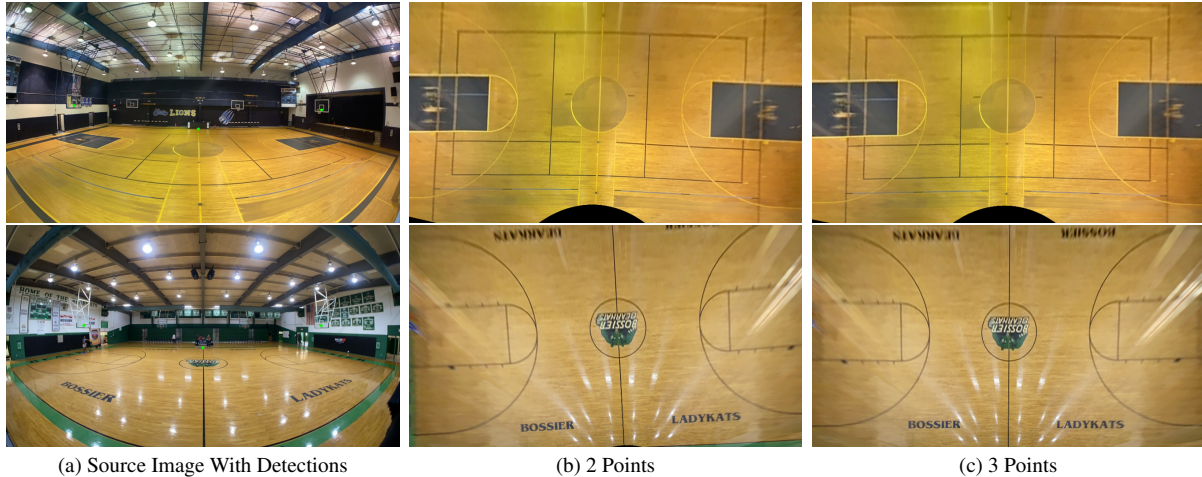


Figure 4. Examples of basketball court registration using the proposed algorithm on point detections. (a) shows the captured image with the green dots marking the three detected landmarks. (b), (c) shows the image projected onto the 3D court ground plane using the estimated camera pose. A good registration aligns the court’s boundaries well with the projected image edges showing a rectified birdseye view of the court. (b) uses two of the detections (backboard rim points) while (c) uses all three

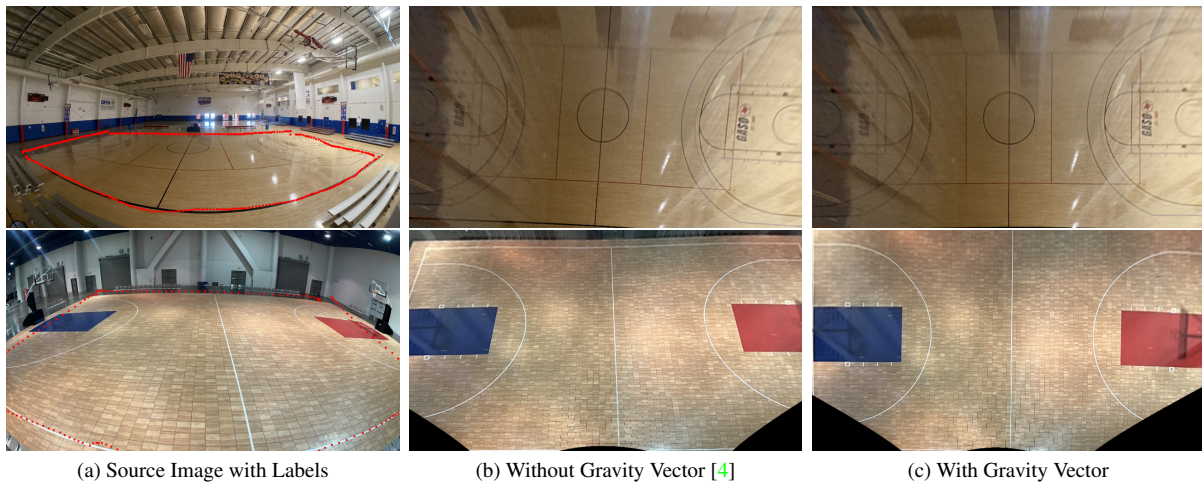


Figure 5. Examples of basketball court registration from lines formed from manually annotated contours. (a) shows the captured image with noisy court boundary annotations marked with red dots. (b), (c) show a similar projection as Figures 4b/4c. (b) estimates pose without the use of the gravity vector while (c) uses the proposed algorithm and is more robust to label noise.

court. We then break this contour using a RANSAC fitting scheme into three or four line segments that correspond with the 3D court boundaries based on perspective. This annotation method extends to any sport with rectangular playing area and is typically easy for users to learn. However, label quality can vary greatly with some labels being quite inaccurate. The gravity vector is utilized here to make the estimation more robust against poor label quality. We note that these line features are an example of a planar configuration as all the objects lie on a ground plane. The faster closed-form solution can therefore be employed which is

advantageous for quickly and more accurately validating RANSAC fittings over a large number iterations. Figures 5b and 5c show qualitative comparisons of court registration from these annotations with and without the gravity vector. Pose estimation without the gravity vector is conducted analytically via the method presented in [4].

7. Conclusion

This paper introduced a novel pose estimation algorithm which leverages axis prior information such as a gravity vector measurement. Incorporating the axis constraint pro-

vides several key benefits over traditional pose estimation methods. These include enabling estimation from fewer feature correspondences, improving robustness to noise, and accelerating iterative pipelines. Extensive experiments validated the algorithm’s accurate and efficient formulation compared to existing techniques. A key advantage of this approach is its ability to accommodate arbitrary combinations of point and line features, which to the authors’ knowledge is a first-of-its-kind capability for axis-constrained pose estimation. Furthermore, the identification of minimal cases and planar configurations enables the use of streamlined closed-form solutions, further boosting performance and differentiating the approach. Finally, the algorithm exhibits superior compute efficiency, especially as the number of inputs scales, outperforming comparative approaches and far surpassing general purpose solutions.

Potential future research directions include exploring alternative loss formulations to automatically balance the loss terms for line features as well as generalizing the approach to handle other projective features like ellipses. Overall, the proposed approach represents a step forward in achieving robust and efficient pose estimation.

References

- [1] Adnan Ansar and Kostas Daniilidis. Linear pose estimation from points or lines. *IEEE Trans. Pattern Anal. Mach. Intell.*, 25:578–589, 2003. [1](#)
- [2] Luigi D’Alfonso, Emanuele Garone, Pietro Muraca, and Paolo Pugliese. P3p and p2p problems with known camera and object vertical directions. In *21st Mediterranean Conf. on Control and Automation*, pages 444–451, 2013. [1](#)
- [3] Johann Grunert. Das pothenotische problem in erweiterter gestalt nebst uber seine anwendungen in der geodasie. In *Grunerts archiv fur mathematik und physik*, pages 238–248, 1841. [1](#)
- [4] Robert Haralick. Determining camera parameters from the perspective projection of a rectangle. *Pattern Recognition*, 22(3):225–230, 1989. [9](#)
- [5] Nora Horanyi and Zoltan Kato. Generalized pose estimation from line correspondences with known vertical direction. In *2017 International Conference on 3D Vision (3DV)*, pages 244–253, 2017. [2](#), [6](#), [8](#)
- [6] Tong Ke and Stergios I. Roumeliotis. An efficient algebraic solution to the perspective-three-point problem. *IEEE Conf. Comput. Vis. Pattern Recog.*, pages 4618–4626, 2017. [1](#)
- [7] Laurent Kneip, Davide Scaramuzza, and Rolande Siegwart. A novel parametrization of the perspective-three-point problem for a direct computation of absolute camera position and orientation. In *IEEE Conf. Comput. Vis. Pattern Recog.*, pages 2969–2976, 2011. [1](#)
- [8] Zuzana Kukelova, Martin Bujnak, and Tomas Pajdla. Closed-form solutions to minimal absolute pose problems with known vertical direction. In *Asian Conference on Computer Vision*, 2010. [1](#)
- [9] Louis Lecrosnier, Remi Boutteau, Pascal Vasseur, Xavier Savatier, and Friedrich Fraundorfer. Camera pose estimation based on pnl with a known vertical direction. *IEEE Robotics and Automation Letters*, 4(4):3852–3859, 2019. [2](#), [6](#), [8](#)
- [10] Vincent Lepetit, Francesc Moreno-Noguer, and Pascal Fua. Epnp: An accurate o(n) solution to the pnp problem. *Int. J. Comput. Vis.*, 81:155–166, 2009. [1](#)
- [11] Landis Markley. Attitude determination from vector observations: A fast optimal matrix algorithm. *Journal of the Astronautical Sciences*, 41, 1993. [6](#)
- [12] Mikael Persson and Klas Nordberg. Lambda twist: An accurate fast robust perspective three point (p3p) solver. In *Eur. Conf. Comput. Vis.*, 2018. [1](#), [6](#), [7](#), [8](#)
- [13] Bronislav Pribyl, Pavel Zemcek, and Martin Cadık. Camera pose estimation from lines using plucker coordinates. In *Brit. Mach. Vis. Conf.*, 2016. [1](#)
- [14] Srikumar Ramalingam, Sofien Bouaziz, and Peter Sturm. Pose estimation using both points and lines for geolocalization. In *2011 IEEE International Conference on Robotics and Automation*, pages 4716–4723, 2011. [1](#)
- [15] Jurgen Richter-Gebert. *Perspectives on Projective Geometry: A Guided Tour Through Real and Complex Geometry*. Springer Science & Business Media, 2011. [4](#)
- [16] Chris Sweeney, John Flynn, Benjamin Nuernberger, Matthew Turk, and Tobias Hollerer. Efficient computation of absolute pose for gravity-aware augmented reality. In *2015 IEEE International Symposium on Mixed and Augmented Reality*, pages 19–24, 2015. [1](#), [6](#), [7](#), [8](#)
- [17] George Terzakis and Manolis Lourakis. A consistently fast and globally optimal solution to the perspective-n-point problem. In *Eur. Conf. Comput. Vis.*, pages 478–494, 2020. [1](#), [3](#), [6](#), [7](#), [8](#)
- [18] Alexander Vakhitov, Jan Funke, and Francesc Moreno-Noguer. Accurate and linear time pose estimation from points and lines. In *Eur. Conf. Comput. Vis.*, pages 583–599, 2016. [1](#)
- [19] Ping Wang, Guili Xu, and Yuehua Cheng. A novel algebraic solution to the perspective-three-line pose problem. *Computer Vision and Image Understanding*, 191, 2018. [1](#)
- [20] Chi Xu, Lilian Zhang, Li Cheng, and Reinhard Koch. Pose estimation from line correspondences: A complete analysis and a series of solutions. *IEEE Trans. Pattern Anal. Mach. Intell.*, 39(06):1209–1222, 2017. [1](#)
- [21] Lipu Zhou, Jiamin Ye, and Michael Kaess. *A Stable Algebraic Camera Pose Estimation for Minimal Configurations of 2D/3D Point and Line Correspondences*, pages 273–288. Springer-Verlag, 2019. [1](#)

PoseGravity: Pose Estimation from Points and Lines with Axis Prior

Supplemental Materials

Akshay Chandrasekhar

A. Proofs

A.1. Solvability of T

Proposition 1: $\sum_i \mathbf{Q}_i^p + \sum_j \mathbf{Q}_j^l$ is invertible for nonzero inputs consisting of at least two linearly independent points, three linearly independent lines, or a linearly independent point and line.

Proof Consider the problem with only $n = 2$ point features \mathbf{p}_0 and \mathbf{p}_1 ($\mathbf{p}_0 \times \mathbf{p}_1 \neq \mathbf{0}$ by linear independence). $\mathbf{Q}_i^p = [\mathbf{p}_i]_{\times}^T [\mathbf{p}_i]_{\times}$ is a real positive semidefinite matrix. Given that $\sum_i \mathbf{Q}_i^p$ is a sum of positive semidefinite matrices:

$$\ker\left(\sum_i \mathbf{Q}_i^p\right) = \bigcap \{\ker(\mathbf{Q}_i^p)\} = \bigcap \{\mathbf{p}_i\}$$

Two linearly independent points are sufficient to ensure $\dim(\ker(\sum_i \mathbf{Q}_i^p)) = 0 \implies \text{rank}(\sum_i \mathbf{Q}_i^p) = 3$ by rank-nullity theorem.

Consider the problem with only $m = 3$ line features ($\mathbf{n}_0 \times \mathbf{n}_1 \neq \mathbf{0}$, $\mathbf{n}_1 \times \mathbf{n}_2 \neq \mathbf{0}$, $\mathbf{n}_0 \times \mathbf{n}_2 \neq \mathbf{0}$ by linear independence). $\sum_j \mathbf{Q}_j^l = \sum_j \mathbf{n}_j \mathbf{n}_j^T$ is the sum of real positive semidefinite rank one matrices:

$$\ker\left(\sum_j \mathbf{Q}_j^l\right) = \bigcap \{\ker(\mathbf{Q}_j^l)\} = \bigcap \{\mathbf{n}_j^\perp\}$$

$$\dim\left(\bigcap \{\mathbf{n}_j^\perp\}\right) = \dim(\ker(\mathbf{N}))$$

where \mathbf{N} is the $m \times 3$ matrix formed by concatenation of the lines. Thus, three linearly independent lines are sufficient for $\text{rank}(\mathbf{N}) = 3$ which implies $\dim(\ker(\mathbf{N})) = \dim(\ker(\sum_j \mathbf{Q}_j^l)) = 0$ and $\text{rank}(\sum_j \mathbf{Q}_j^l) = 3$.

Consider the problem with $n = 1$ point \mathbf{p}_0 and $m = 1$ line \mathbf{n}_0 ($\mathbf{p}_0 \cdot \mathbf{n}_0 \neq 0$ by linear independence). Using the fact that \mathbf{Q}_0^p and \mathbf{Q}_0^l are real positive semidefinite matrices:

$$\ker(\mathbf{Q}_0^p + \mathbf{Q}_0^l) = \ker(\mathbf{Q}_0^p) \cap \ker(\mathbf{Q}_0^l) = \{\mathbf{p}_0\} \cap \{\mathbf{n}_0^\perp\}$$

Thus, $\dim(\ker(\mathbf{Q}_0^p + \mathbf{Q}_0^l)) = 0$ since \mathbf{p}_0 and \mathbf{n}_0 are linearly independent, and $\text{rank}(\mathbf{Q}_0^p + \mathbf{Q}_0^l) = 3$.

Consider the problem with n points and m lines:

$$\begin{aligned} \ker\left(\sum_i \mathbf{Q}_i^p + \sum_j \mathbf{Q}_j^l\right) &= \left\{ \bigcap \{\mathbf{p}_i\} \right\} \cap \left\{ \bigcap \{\mathbf{n}_j^\perp\} \right\} \\ &= \mathbf{p}_0 \cap \dots \cap \mathbf{p}_{n-1} \cap \mathbf{n}_0^\perp \cap \dots \cap \mathbf{n}_{m-1}^\perp \end{aligned}$$

If there exists a subset of features matching one of the three previous cases, then using the associativity and commutativity of intersection, we can intersect those objects together first creating a trivial kernel $\ker(\mathbf{Q})$. Intersecting this kernel with any other kernels would ensure $\dim(\ker(\sum_i \mathbf{Q}_i^p + \sum_j \mathbf{Q}_j^l)) = 0$, extending the solvability to arbitrary supersets of these point and line features.

A.2. Loss Conic Rank for Minimal Problems

Proposition 2: For any nonzero, linearly independent, and minimal ($n + m = 2$, $n \geq 1$) inputs, $\text{rank}(\mathbf{\Omega}) \leq 1$.

Proof It can be assumed without loss of generality that image point \mathbf{p}_0 corresponds to the 3D point $\mathbf{d}_0 = (0, 0, 0)$ since the translation estimate is relative and each configuration has at least one point that can define the new coordinate frame origin.

Consider the problem with $n = 2$ points \mathbf{p}_0 and \mathbf{p}_1 . The expression for loss conic can be expanded and simplified to the following:

$$\begin{aligned} \mathbf{\Omega} &= (\mathbf{A}_1^p)^T \mathbf{Q}_1^p \mathbf{A}_1^p - (\mathbf{Q}_1^p \mathbf{A}_1^p)^T (\mathbf{Q}_0^p + \mathbf{Q}_1^p)^{-1} \mathbf{Q}_1^p \mathbf{A}_1^p \\ &= (\mathbf{A}_1^p)^T (\mathbf{Q}_1^p - \mathbf{Q}_1^p (\mathbf{Q}_0^p + \mathbf{Q}_1^p)^{-1} \mathbf{Q}_1^p) \mathbf{A}_1^p \\ &= (\mathbf{A}_1^p)^T \mathbf{K} \mathbf{A}_1^p \end{aligned}$$

Examining the matrix \mathbf{K} , we see that $\mathbf{p}_1 \in \ker(\mathbf{K})$. Non-trivially, we can verify by calculation that $\mathbf{p}_0 \in \ker(\mathbf{K})$ as well. Since the two points are assumed linearly independent, $\dim(\ker(\mathbf{K})) \geq 2$, so $\text{rank}(\mathbf{K}) \leq 1$. Multiplication by \mathbf{A}_1^p can only maintain or decrease the rank of the product, so $\text{rank}((\mathbf{A}_1^p)^T \mathbf{K} \mathbf{A}_1^p) = \text{rank}(\mathbf{\Omega}) \leq 1$.

Consider the problem with $n = 1$ point \mathbf{p}_0 and $m = 1$ line \mathbf{n}_0 . The expression for loss conic similarly can be expanded and simplified to the following:

$$\begin{aligned} \mathbf{\Omega} &= (\mathbf{A}_0^l)^T (\mathbf{Q}_0^l - \mathbf{Q}_0^l (\mathbf{Q}_0^p + \mathbf{Q}_0^l)^{-1} \mathbf{Q}_0^l) \mathbf{A}_0^l + \mathbf{V}_0^T \mathbf{Q}_0^l \mathbf{V}_0 \\ &= (\mathbf{A}_0^l)^T \mathbf{L} \mathbf{A}_0^l + \mathbf{V}_0^T \mathbf{Q}_0^l \mathbf{V}_0 \end{aligned}$$

Nontrivially, we can verify by calculation that \mathbf{L} is the zero matrix. $\text{rank}(\mathbf{Q}_0^l) = 1$ and multiplication by \mathbf{V}_0 can only maintain or decrease rank, so $\text{rank}(\mathbf{V}_0^T \mathbf{Q}_0^l \mathbf{V}_0) = \text{rank}(\mathbf{Q}_0^l) \leq 1$.

Intuitively, this result stems from the fact that minimal configurations constrain four degrees of freedom while the estimation problem has six degrees of freedom. Estimation of \mathbf{T} consumes three of those constraints, so there is only one left when constructing \mathbf{Q} . The problem is solved by applying the additional constraints to solution \mathbf{r} that $x^2 + y^2 = 1$ and the third element of \mathbf{r} is 1. Also note that the eigenvector corresponding to the nonzero eigenvalue of \mathbf{K} when $\text{rank}(\mathbf{K}) = 1$ is $\mathbf{p}_0 \times \mathbf{p}_1$ which defines the projective line between the points, playing a similar role to \mathbf{n}_0 in \mathbf{Q}_0^l .

A.3. Recovery of Non-Exact Minimal Solutions

Proposition 3: *If the zero level curve of a rank one loss conic in the x - y plane exists and has no real solutions with the unit circle, then the best feasible loss-minimizing solution is the point on the circle closest to the curve.*

Proof The rank one loss conic is represented as $\mathbf{r}^T \mathbf{Q} \mathbf{r} = (l^T \mathbf{r})(l^T \mathbf{r}) = 0$ for some line $l = [a, b, c]^T$. The distance between the line and some point $q_p = [q_x, q_y, 1]^T$ in the x - y plane is given as:

$$\text{dist}(l) = \frac{|aq_x + bq_y + c|}{\sqrt{a^2 + b^2}}$$

$$\text{dist}(l)^2 = \frac{(l^T q_p)(l^T q_p)}{a^2 + b^2}$$

The distance squared from a point to a line is the original loss function scaled by a constant. Therefore, minimizing the distance (and thereby distance squared) minimizes the loss function. Since the line is assumed to not intersect any point on the unit circle, the best feasible solution is the point on the circle closest to the line. Obtaining l from conic decomposition, this solution can be simply calculated as:

$$\mathbf{r} = \left[\frac{-a}{\sqrt{a^2 + b^2}} \quad \frac{-b}{\sqrt{a^2 + b^2}} \quad 1 \right]^T$$

If $a = b = 0$, the conic does not exist in the x - y plane and a uniquely loss minimizing solution cannot be found.

B. Note on Line Loss Scale δ

For line features, the proposed solver’s loss function combines the rotation and translation loss terms instead of estimating them sequentially like other approaches. However, since those two terms in loss function in equation 16 have different 3D objects associated with them, there can be a bias from the points \mathbf{m}_j and the line directions \mathbf{v}_j having different scales (e.g. if \mathbf{v}_j is normalized), leading to the loss being dominated by one term and resulting in suboptimal pose estimates. Estimates from planar configurations

are particularly sensitive to this scale difference. This issue does not occur when dealing only with point features as the loss is encapsulated in a single term that includes both rotation and translation components in a naturally balanced way. To compensate for the bias, we found it sufficient to introduce a constant scaling factor δ^2 which manually balances the line direction loss. In our experiments, we use $\delta = 100$ with normalized directions \mathbf{v}_j for standardization.